Land subsidence, sea level rise, and enhanced tidal intrusion: unveiling the land loss and nuisance flooding potential in the Barataria Basin, Louisiana

Byungho Kang[1], and Surui Xie[1]

[1]Department of Civil and Environmental Engineering, University of Houston, Houston, TX, USA

Corresponding author: Byungho Kang (bkang2@central.uh.edu)

Key Points:

- We found a persistent increase in landward tidal attenuation in the Barataria region, indicating an increased risk of tidal intrusion over time.
- We inferred significant land subsidence rate changes with historically mapped land areas.
- By 2045, high tides will increase Barataria's land inundation, widening the land area gap between MSL and MHHW.

Abstract

This study investigates land loss and coastal inundation in Louisiana's Barataria Basin, a region highly susceptible to anthropogenic pressures and natural factors like land subsidence, sea-level rise, and tidal dynamics. Using high-resolution Digital Elevation Models (DEM) and water level data from the Coastal Reference Monitoring System (CRMS) stations, we analyzed changes in land area and water levels between 2007 and 2022. The attenuation coefficient magnitude of tidal intrusion, which quantifies tidal amplitude reduction as a function of landward distance from the coastline, exhibited a persistent decrease from 2007 to 2022 for O1 and K1 (the dominant tidal constituents), with an accumulated decrease of nearly 20%, signaling enhanced hydrological connectivity across the region. We also projected land area for historic years and predicted it for future years up to 2075, based on a range of displacement rates to account for uncertainties in vertical land motion. Our analyses predict that, in the absence of human intervention, the significance of tidal variations in influencing land loss will escalate; by 2045, the land area estimated based on Mean Higher High Water (MHHW) will constitute approximately 65% of the land area estimated using Mean Sea Level (MSL). Our findings underline the importance of considering the compound effects of subsidence, sea-level rise, and tidal dynamics in future land loss mapping and flood risk assessments.

Plain Language Summary

Sea-level rise, land subsidence, and tidal dynamics are key factors contributing to land loss and increased flooding risks. To estimate the vulnerability of flooding in Barataria, Louisiana, we analyzed long-term water level records, elevation data and conducted predictive simulations. Our analysis revealed a decrease in tidal attenuation, indicating that tides are propagating more efficiently through the inland area. This finding suggests that tidal forces could exacerbate the already challenging issues of land loss and flooding. We also found that the assumptions made about land subsidence rates can significantly affect the accuracy of historic land area projections. Using certain rates led to overestimations, highlighting the challenges of measuring subsidence rates that can vary over time. We estimated land areas susceptible to inundation under normal tide conditions for past and present scenarios. For future predictions, we extended our analysis to include high-tide scenarios. We found that if sea level continues to rise at it’s current rate and land subsidence proceeds at its current rate, the inclusion of high tides becomes a key factor in identifying areas at risk of flooding.

Keywords: Tidal Variability, Sea Level Rise, Land subsidence, Inundation, Hydroconnectivity

1 Introduction

Coastal Louisiana’s wetlands, often recognized as one of the most crucial environments in the United States (Couvillion et al., 2016), serve invaluable ecological functions. These include providing habitats for critical species, acting as a protective barrier against storm surges, enhancing water quality through nitrate removal, et cetera (Cheng et al., 2020; Vaccare et al., 2019). Economically, these wetlands held an estimated value of US$140,000 per hectare per year in 2011 (Costanza et al., 2014), a figure that has likely increased in recent years. The coast protects the infrastructure that delivers 90% of the nation's outer continental oil and gas, a significant source that constitutes 20% of the total national oil and gas supply (Couvillion et al., 2016; CPRA, 2018).

The Barataria Basin is an essential wetland within Louisiana's Gulf region. Central to the Gulf's fisheries species, it accommodates an estimated 97% of all commercially valuable species that rely on both this basin and adjacent coastal estuarine basins for some or part of their life cycle (Nelson et al., 2002). This role translates to a significant contribution to the nation's commercial seafood harvest, constituting 20% of the United States' yield, or approximately 500 million pounds of fish and shellfish annually (Nelson et al., 2002). However, despite its rich biodiversity and economic significance, the Barataria Basin is losing land at an alarming rate. This basin accounts for ~25% of all land loss in the Mississippi Delta Plain (Edmonds et al., 2023) and lost nearly 1,100 km^2 of wetland area between 1932 and 2016, roughly 30% of its original size (Couvillion et al., 2017).

This land loss is driven by a combination of natural processes such as land subsidence due to crustal loading and gravitational compaction, sea-level rise, and the decrease in the accretion of fluvial sediment on the coastal marsh (Bowman et al., 1995; Inoue et al., 2008; Karegar et al., 2015). However, recent studies reveal how human interventions, such as hydrologic alteration and resource extraction, significantly exacerbate these natural processes in the Barataria region (Edmonds et al., 2023). For example, man-made dams and levees along the Mississippi River, originally built to protect the city from flooding, have significantly reduced sediment deposition. The consequences include accelerated land loss and saltwater intrusion. To address the sediment deficit, the Mid-Barataria Sediment Diversion (MBSD) project, which aims to redirect sediment-rich river water into the Barataria Basin, received approval from the authority in 2022. This multibillion-dollar project is expected to reestablish deltaic processes and expand the wetland area over the next few decades, in the hope of reaching a peak increase of 17,300 acres by 2050 (USACE, 2022). However, the project's effectiveness largely depends on its ability to keep pace with future subsidence and sea-level rise (Törnqvist, 2023).

Among the many factors that are contributing to the land loss and flooding in the Barataria Basin, tidal influences are sometimes underdiscussed yet critical. Despite the Gulf coast's relatively small tidal ranges (Gornitz et al., 1991), their impact on the submergence of the flat and low-lying land areas is escalating due to rapid eustatic sea-level rise and coastal subsidence (Holzer et al., 1984; Sweet et al., 2018; Yang et al., 2014). Current projections predict significant increases in minor high tide flooding over a 10-year period by the 2030s (Thompson et al., 2021). Given these concerns, it becomes vital to accurately predict the impact of coastal inundation for effective hazard mitigation and strategic planning (Mostafiz et al., 2021). While much research has focused on flood risk assessment based on individual factors such as sea level rise (SLR) or land subsidence (Mostafiz et al., 2021), less is known about the region's overall susceptibility to land loss, especially that resulting from high tide-induced flooding.

In this study, we investigated the susceptibility to land loss and flooding by establishing a baseline scenario to understand the natural progression of land loss in the Barataria Basin without human intervention. We first analyzed the characteristics of tidal intrusion in the Barataria region, examining how tidal intrusion evolves over time due to increased water connectivity and predicting future water highs associated with ocean tides. By estimating the extent of land area through reversing SLR and vertical land motion and comparing it with the historical land area data, we derived plausible mean land subsidence rates over the past 80 years 1932 to 2014. Based on the SLR and land subsidence, along with the changes in tidal intrusion, we predicted future land area changes during high tides.

2 Environmental Setting

2.1.Geographical Characteristics of the Study Site

The Mississippi Delta Plain (MDP), a region of considerable economic and ecological value, had a net growth in area over several millennia following the stabilization of sea levels (Day et al., 1997). This growth was caused by various natural factors, such as storm events, river flooding leading to sediment deposition, and the reshaping of distributary channels (avulsions) (Roberts, 1997). However, this trend was interrupted by escalating human activities in the 20th century, resulting in significant wetland loss in coastal Louisiana (Gagliano et al., 1981). Some of these human activities include the construction of levees and the closure of distributaries, which hinder the sediment supply from the Mississippi River to the MDP (Blum et al., 2009), along with alterations in hydrology caused by canal construction (Day et al., 2000).

Within this broader context of the MDP, the Barataria Basin serves as an important example of the region's susceptibility to land loss due to anthropogenic pressure. The Barataria Basin is a vast interdistributary zone located west of the Mississippi River delta, with a total area of approximately 7,100 km^2. The elevation within the basin varies within only 5 m, with high natural levees by the Mississippi River at 4 to 5 m, and marshes near sea level (Byrnes et al., 2019); the average depth of the estuary is about 2 m (Das et al., 2012).

In this study, we focused on the areas excluding the Fastlands, where there is dense infrastructure such as levees to protect local human communities and the agricultural lands. Thus, our analysis primarily focuses on a reduced area of 5,700 km^2, bordered by the Mississippi River to the east and north, the Bayou Lafourche to west, and the Gulf of Mexico to the south (Figure 1).

We divided the study area into two regions based on the intensity of tidal influence: a northwestern wetland habitat featuring fresh water marshes with several large lakes that have small tidal influence (upper Barataria) and a southeastern zone composed of brackish water and marshes that are connected to the Gulf of Mexico via four tidal passes (lower Barataria) (Das et al., 2012).

2.2 Hydrological Characteristics and Analysis

To accurately characterize the tidal intrusion in the Barataria region, it's important to comprehend the tidal spectrum in the region. We determined the characteristics of ocean tide variations primarily through the data collected by the Grand Isle tidal gauge (29.263 N, 89.957 W; NOAA station ID: 8761724). This gauge was established in 1979, but full records of hourly water elevation were not available until 1981. This study used quality-controlled records from 1981–2022 (Figure 2a). We calculated a relative sea level rise (RSLR) rate of 8.3 mm/yr at this tide gauge, slightly slower than the 9.16 ± 0.37 mm/yr local sea level trend averaged from 1947 to 2022 by NOAA. The average vertical motion rate of the GPS monument at Grand Isle derived from nearly two-decades of continuous measurements is -6.3 ± 0.4 mm/yr (Karegar et al., 2020). These rates are consistent considering different data spans and the vertical rate difference between benchmarks anchored at different depths (e.g., the near-surface Holocene sediment compaction rate is a function of foundation depth). Nevertheless, in this study, we adopted a eustatic sea-level rise rate of 3 mm/year for the Gulf of Mexico. The rate represents a slight increase from the 2.9 ± 0.4 mm/year determined by satellite altimetry data from 1992 to 2014, as it accounts for recent accelerations in sea-level rise (Pahl, 2017).

After detrending the water elevation time series based on the RLSR rate, we analyzed annual tide constituent of the Grand Isle water elevation records using T-Tide (Figure 2b; Pawlowicz et al., 2002). The F-ratios, calculated as the ratio of amplitudes (K1+O1) / (M2+S2), fall between 8 and 13 at Grand Isle, indicating a strong dominance of the diurnal tidal component over the semi-diurnal component. Further, comparison of tidal analyses using the data collected by CRMS water stations 0231 and 0273 with those collected at Grand Isle indicated that within the diurnal tidal spectrum, the O1 and K1 constituents are the major tidal components, characterizing the tidal behavior in the region. Furthermore, we applied T-Tide to the detrended time series depicted in Figure 2a to evaluate the temporal variations in the amplitude of diurnal tide constituents at Grand Isle. Notably, the results reveal the influence of the 18.6-year lunar nodal cycle (Figure 2c).

3 Material and Methods

3.1. Water Level and Land Elevation Data

To analyze local water level changes, we used the continuous water level data collected between 2007–2022 from selected Coastal Reference Monitoring System (CRMS) stations that were located across coastal Louisiana. We focused on a subset of 91 monitoring stations from the Barataria basins that recorded hourly water elevation measurements (Figure 1a). This selection comprised 49 CRMS stations near inlets (lower Barataria) and 42 CRMS stations situated further from the sea (upper Barataria).

As part of data quality assurance, water elevation records were corrected to mitigate issues related to biofouling and instrument drift, and erroneous data points were removed by the data provider (CPRA, 2022). Also, the raw water levels were recorded in orthometric heights, with the geoid model transitioning from geoid 99 to geoid 12A on September 30th, 2013. To align the measurements with a consistent height datum for each CRMS location (using geoid 12A), we applied a small correction specific to each CRMS location.

We used data from 40 CRMS stations equipped with the surface-elevation table–marker horizon (RSET-MH) instruments within Barataria to consider vertical land motion rate. The subsidence rates were adopted from the study by Jankowski et al. (2017), which provided estimations factoring in both shallow subsidence rates (organic matter decomposition in the uppermost sediment layers, sediment compaction, and vertical accretion) and deep subsidence rates (glacial isostatic adjustment, tectonic processes, fluid withdrawal, etc).

To estimate the change in land area, we utilized a Digital Elevation Model (DEM) derived from the Coastal National Elevation Database (CoNED) topobathymetric digital elevation models (TBDEMs) developed from measurements collected in 2014 for the land height (Figure 3a). This comprehensive model integrates both topographical (land elevation) and bathymetric (water depth) representations, providing the highest resolution elevation model for the region among public-available DEMs. The vertical datum used for the DEM was North American Vertical Datum 1988 (NAVD88), with a geoid model of 12B. We confirmed that within the study area, there were no significant disparities between the use of geoid 12A and

12B. While the original horizontal resolution of the CoNED TBDEMs was 3 m, we downsampled it to 5 m to reduce the computational load of our analyses.

3.2 Sea Level and High Water Measurement and Prediction

To simplify the notation within our study, we define the Mean Sea Level (MSL) for a given year as the average water elevation during that year. Also, we define the Mean Higher High Water (MHHW) of a year as the average of daily maximums throughout the year (note that MHHW traditionally refers to the higher high water average over an 18.6-year period). We measured both MSL and MHHW for each observational year from 2007 to 2022 at every CRMS station across the Barataria region.

Meanwhile, we took a specific approach for predicting the future MHHW at each CRMS location to ensure the accuracy of the MHHW prediction for each year. Tidal analysis of the data suggests that the 18.6-year nodal cycle clearly affects the tidal amplitudes. However, as we lack CRMS water elevation observations for the entire tidal modulation cycle, and the CRMS stations occasionally miss observations, it is inappropriate to extrapolate future tidal highs by applying the tidal modulation directly to O1 and K1 amplitudes for each of CRMS stations. We addressed this by leveraging the relationship between the Grand Isle tidal gauge (reference station) and each CRMS station.

Using T-tide, we first measured the annual amplitude and phase of the dominant diurnal tide constituents, namely O1 and K1, for each CRMS station throughout 2006 to 2022 where we set the Rayleigh resolution limit at 5 (Pawlowicz et al., 2002). From the amplitude of the same tide constituents measured at the tide gauge in Grand Isle, we calculated the ratio, R_i (Y), between the reference station and each CRMS station i for a given year Y based on tidal admittance relations.

Specifically, the ratios can be denoted as:

$$R_{i,O1}(Y)=\frac{C_{i,O1}(Y)}{G_{O1}(Y)} \quad \text{and} \quad R_{i,K1}(Y)=\frac{C_{i,K1}(Y)}{G_{K1}(Y)} \tag{1}$$

where $C_{i,O1}(Y)$ and $C_{i,K1}(Y)$ represent the amplitudes of O1 and K1 for the i-th CRMS station, and $G_{O1}(Y)$ and $G_{K1}(Y)$ refer to the respective values at the Grand Isle tidal gauge.

Using the obtained ratio of $R_{i,O1}$ and $R_{i,K1}$, we predicted the O1 and K1 amplitude of each of CRMS station $\widehat{C}_{i,O1}(Y)$ and $\widehat{C}_{i,K1}(Y)$ for an arbitrary future year Y as follows:

$$\widehat{C}_{i,O1}(Y)=R_{i,O1}(Y)\times\widehat{G}_{O1}(Y) \quad \text{and} \quad \widehat{C}_{i,K1}(Y)=R_{i,K1}(Y)\times\widehat{G}_{K1}(Y) \tag{2}$$

where $\widehat{G}_{O1}(Y)$ and $\widehat{G}_{K1}(Y)$ are expected future values of O1 and K1 amplitude for the Grand Isle tidal gauge at the future year Y, by fitting sinusoids with 18.6-year period to each of annual pattern for O1 and K1 constituents (see Figure 2c). As it was uncertain at this point whether the ratio between reference and each of CRMS stations $R_{i,O1}(Y)$ and $R_{i,K1}(Y)$ are constant throughout different years, we tracked how each of these ratios changed over time which is discussed in section 4.1.

On the other hand, as the 18.6-year nodal correction was not applied in this analysis in order to assess the influence of nodal modulation on tidal amplitude, Greenwich phase for each constituent had the periodic fluctuation. Accordingly, we derived predictions for the Greenwich phase of each tidal constituent for each year, denoted as $\theta^{Y}_{i,O1}$ and $\theta^{Y}_{i,K1}$, based on the 18.6-year cycle for each CRMS station.

Based on estimated amplitude and phase of O1 and K1 tide constituent, we synthesized the tidal elevation throughout the year Y with the same hourly interval for the observation.

$$\eta_i(t)=\widehat{C}_{i,O1}(Y)\sin(2\pi f_{O1}t+\theta^{Y}_{i,O1})+\widehat{C}_{i,K1}(Y)\sin(2\pi f_{K1}t+\theta^{Y}_{i,K1}) \quad (3)$$

Where f_{O1} and f_{K1} are frequencies of O1 and K1, respectively.

We defined mean of daily maxima of $\eta_i(t)$ throughout the year Y as η^{Y}_{i}, where we can derive the predicted MHHW at the year Y for each of CRMS as:

$$\zeta^{Y}_{i}=c_i+\kappa\,(Y\text{-}2022)+\eta^{Y}_{i} \quad (4)$$

Where c_i represents MSL for year 2022, the latest observation year, κ is the rate of eustatic SLR, set at 3 mm/yr (Pahl, 2017) .

3.3 Interpolation

In the process of estimating the MSL and MHHW for the entire study area, we employed the ordinary Kriging method. We used a linear model, a+bx, in which the maximum distance was set to 60 km and lags for semivariance were fix at 2 km intervals. The selection of these parameters was based on the spatial characteristics observed in the semivariogram. Likewise, the vertical land motion rate for the region was also determined using the ordinary Kriging method (Figure 3b). The linear model was used with the same parameters; lags for semivariance were set at 2 km and the maximum distance was kept at 60 km.

To generate a more realistic interpolation map, we removed several outliers before data interpolation. Specifically, we identified and excluded two outlier values, each of which exceeded the mean vertical land motion rate for the region by more than three standard deviations. This ensured that our estimates of vertical land motion rates across the region were not disproportionately influenced by possible local effects.

3.4. Land area estimation: DEM thresholding

The main objective of this study is to calculate the land area changes of the Barataria region in different intervals. Our methodology involved subtracting or adding the expected cumulative vertical land motion, calculated from the time of the DEM measurement in 2014, from the land height of DEM measurements. Due to limitations in measuring the total subsidence caused by both the deep and shallow processes, different measurement techniques sometimes produce seemingly conflicting results. For example, the subsidence rate map from Nienhuis et al. (2017), based on RSET measurements by Jankowski et al. (2017), indicates rates ranging from 6 mm/yr in upper Barataria to 12 mm/yr in lower Barataria. However, Byrnes et al. (2019) report a range of 2 to 7 mm/yr using GPS-derived data. The divergence arises because GPS-derived subsidence rate reflects the vertical motion rate of the monument, which is usually anchored deep into the sediment. In contrast, the RSET-MH method tracks the vertical position of the surface with respect to a rod driven deeply into the sediment, hence the data only reflect the vertical displacement rate of the upper layer. To overcome the discrepancies caused by the inherent limitations of different techniques, we predict the vertical land motion based on a range of plausible displacement rates.

We considered cumulative vertical land motion based on both full and a halved subsidence rate of Figure 3b. This provided us with two sets of adjusted land height estimations, where these adjusted land height estimates were then compared with an interpolated map of either the MSL or MHHW. Through this comparison, we estimated the land area above the surface water at different times.

In land area estimation, we utilized a 'bathtub' inundation model based on two rules (Poulter et al., 2008; Yunus et al., 2016): the 'zero-pixel connectivity' and 'four-way pixel connectivity'. The former involves flooding rasters lower than sea level (either MSL or MHHW), thus estimating the maximum impact of such inundation. In contrast, the latter rule provides a more detailed view of coastal flooding, whereby rasters are flooded only if they are lower than sea level and directly connected to open water.

In our specific projections for the MSL maps for historic years (1932, 1955, 1975, and 1999), we used the MSL map that was interpolated for 2014 as the reference. Since we do not have observations for the earlier years, we subtracted the cumulative Sea Level Rise (SLR) for each specific year from each raster of the 2014 map. This approach enabled us to create estimated MSL maps for the specified past years, relying solely on the 2014 data. By comparing the resulting MSL map with the adjusted land height—based on either the full or halved land subsidence rate—we estimated the extent of the land area.

For the land area estimation of future years 2045 and 2075, we predicted for both MSL and MHHW maps. For the MSL map prediction, we added the expected cumulative SLR to each raster in the interpolated 2022 MSL map, using our most recent data on mean sea level. On the other hand, as outlined in section 3.2, we predicted the MHHW at each of the CRMS stations which we interpolated MHHW map for the years 2045 and 2075, for the sake of accurate prediction of future high tide levels. In both cases, we accounted for cumulative vertical land motion by subtracting it from the DEM land height.

4.Results and discussion

4.1. MHHW Prediciton

4.1.1. Tidal Modulation of Amplitude

During the CRMS observation span, from 2006 to 2022, we found substantial influence of tidal modulation on the amplitude of diurnal constituents (O1 and K1) at coastal CRMS stations. Figure 4a shows how O1 amplitude changes during the observation span, with similar patterns found for K1 amplitude.

The O1 amplitudes for most of the coastal CRMS stations exhibited a fluctuation of around 3-4 cm per modulation cycle. While the value itself is small, the combined modulation with the K1 amplitudes modulation, which has similar amount of modulation during the cycle, could be pivotal for determining land inundation, especially for low relief regions near sea level. However, this fluctuation diminishes with increased distance from the coast. CRMS stations around the upper and lower Barataria boundaries, located approximately 50 km from the coast, exhibited reduced modulations around 1-2 cm. The most distant stations from the coast exhibited near-zero modulations, implying that both the amplitudes of diurnal constituents itself and the impact of nodal modulation are limited for inland CRMS stations.

Figure 4b shows the notable fluctuations in O1 amplitude at coastal CRMS stations, moving from 13 cm in 2008 to 10 cm in 2014, and then to 14 cm in 2022. Additionally, the figure illustrates that the relationship between distance from coastline (d_i) to each of CRMS stations and O1 amplitudes for each station ($C_{i,O1}$) can be modeled by the exponential function, $y=\alpha\times\exp(\beta\times x)$, where x is the distance used in the fitting function, α is the baseline coefficient and β is the attenuation coefficient. It is important to note that in this study, the term 'magnitude' is used to describe the absolute value of the attenuation coefficient, which is intrinsically negative.

The fitted curves varied annually throughout the observation span, showing how tidal modulation leads to significant amplitude change: The lowest modulation cycle around 2015 year showed curve closest to the origin, while the higher modulation cycle around 2006 or 2022 had curves farther from the origin. In contrast, exponential curves, representing the relationship between the station distance (d_i) and the corresponding ratio of O1 amplitudes ($R_{i,O1}$), demonstrated almost consistent outward shift throughout the observation years from 2006 to 2022 (Figure 4c). This increase in amplitude ratios indicates a growing tidal influence of the region, extending beyond the coast into the inland areas. Furthermore, the ratio values at some coastal CRMS stations, equivalent to the baseline coefficient α exceeded 1, possibly due to their locations in the estuary's shallower regions. The local geomorphic characteristics may increase friction with the bottom, hindering the outgoing tide and leading to a larger difference between high and low tides in the estuary relative to the adjacent open sea.

4.1.2. Predicting Future Influence of Tidal Modulation

The increasing effect of tidal intrusion in coastal and inland waters calls for additional consideration on changes in tidal influence over time. We observed different temporal patterns in the baseline coefficients (α) and the attenuation coefficient (β). Here, the baseline coefficients of annual exponential fit model did not show any significant trend overtime (Figure 5a). As discussed in the previous section, the values are typically higher than 1 and bounded by 1.2 for O1 and 1.3 for K1 tide constituents, indicating larger tidal range of Coastal CRMS station than the Grand Isle tidal station.

On the other hand, we observed strong evidence of decreasing attenuation coefficient magnitude over time (Figure 5b). The annual attenuation coefficient magnitude of O1 constituent decreased from 0.034 in 2007 to 0.028 in 2022 (18% decrease), while the same magnitude of K1 constituent decreased from around 0.036 in 2007 to around 0.028 in 2022 (22% decrease). We note that this continual decrease of attenuation magnitude can not be explained solely by the 18.6-year nodal modulation as the trend spanned not just the rising nodal modulation period (around 2017 to 2022), but also the falling tide (around 2008 to 2017). Hence, this observed trend of decreasing attenuation magnitude suggests a diminishing effect of tidal attenuation, which likely related to a progressive decrease of natural geographical or terrain barriers that has led to enhanced hydrological connectivity across the region.

As there were no significant trend for the baseline coefficients, we simply assumed the mean of baseline coefficients throughout the observation span as the estimate of future baseline coefficient and extrapolated the ratio amplitude based on increasing attenuation coefficient. We found substantial increase in the ratio, particularly at the 50 km boundary, where the ratios of both tidal constituents are expected to surge from 0.2 in 2022 to around 0.8 in 2075 (Figure 5c). Even the most inland CRMS stations have increased ratios around 0.5 in 2075, though these estimates may be overestimated by the assumption that is based on continuous increase of the attenuation coefficient. In reality, however, it is more likely that the rate of attenuation coefficient increase (or the magnitude decrease) will change over time if tidal intrusion pattern has changed. The change of ratios highlights a growing influence of diurnal tidal amplitude on regional hydrodynamics, particularly regarding high tides and inundation processes. Therefore, future evaluations of land susceptibility to flooding should consider this increasing tidal impact, along with traditional factors such as SLR and vertical land motion. Figure 6 illustrates the effect of tidal variations on flooding. The elevated tidal amplitudes will increase the risk of coastal flooding such that a larger portion of the coastal land will be flooded temporarily during tidal highs (the light blue shade in Figure 6).

4.2. Land Area Projection for Past

We estimated the historic land area using the MSL map in comparison to the adjusted DEM vertical height. The land area defined by the DEM above the MSL, measured at 2,376 km^2 for zero-connection (Figure 7a). Also, the default DEM value above 0 m in NAVD 88, without considering the water level or subsidence, measured the land area at 2,487 km^2 for zero-connection. Both of these estimates are smaller than the Landsat measurements, which recorded a land area of 2,656 km^2 in August 2014. The mismatch between DEM-based land area estimates and Landsat measurements can be partially explained by the local sea level relative to the height datum, and the different characteristics in LiDAR DEM and Landsat optical imagery, as LiDAR can penetrate vegetation and Landsat data reflect the canopy area.

The projected past land area based on the original vertical land motion rate was significantly larger than the mapped land area with historic surveying data (Figure 7a). This suggests that the overall land subsidence rate derived from data collected from as early as 2005 and as late as 2009 to 2015 (Jankowski et al., 2017) is likely much higher than the mean land subsidence rate over the past 80 years throughout the region. In contrast, the estimated land area for the MSL, assuming a halved rate of vertical land motion, agrees reasonably well with the rate of land loss with the Landsat measurement, particularly from 1975 to 2014 (Figure 7a). This halved rate of approximately 4.8 mm/yr in Grand Isle (9.6 mm/yr in Figure 3a) correlates well with the estimated land motion rate of around 5.3 mm/yr in the Grand Isle tidal station reported in Section 2.2. Nevertheless, it should be noted that the RSLR of the Grand Isle from 1940 to 1980 was inferred to be similar to, or even greater than, the RSLR from 1980 to 2022, while using the halved land motion rate for projections prior to 1975 leads to a significant discrepancy between observed and projected land areas (Figure 7a). These conflicting outcomes could stem from anthropogenic activities such as oil and gas extraction, which have exerted a significant impact on landward subsidence rates since the early 1970s. Temporal fluctuations in the relative sea-level rise (RSLR) and vertical motion rate at the Grand Isle station are largely attributable to these extraction activities (Day et al., 2020; Kolker et al., 2011). Notably, given the inherent susceptibility of wetland marshes to subsidence due to their organic-rich soils and hydrological sensitivity, the historic oil and gas extraction activities, primarily located landward, may disproportionately affect landward areas featuring wetland marshes more than coastal regions like Grand Isle. On the other hand, ignoring land vertical motion completely and considering SLR only led to a considerable underestimation of land area, indicating that processes other than SLR contributed to a significant portion of the observed land area decrease from 1932 to 2014.

Figure 7b shows the projected land areas from 1932 to 2014. When comparing with Figure 1b, even a halved subsidence rate could lead to some overestimation of the past land loss. For instance, our projection shows almost the entire Eastern Southern part of the Barataria region as land in 1932 (Figure 7b), contradicting the observation that showed scattered water bodies (Figure 1b). While land area projection based on MSL and the halved vertical land motion rate aligned well with the observed land loss in the outer region near the fastland in Southern Baratarias between 1956 and 1975, areas near the sea showed a notable mismatch. The observed land loss near the ocean from 1975 to 1999 corresponded more closely with the projected land loss than the period from 1955 to 1975. Furthermore, it was projected that Lac des Allemands as land before 1999, and Lake Cataouatche and Lake Salvador as land before 1955. However, historical data suggest only a slight decrease in land area within these regions. These disparities might be attributed to DEM errors at low heights, nonsteady nature of vertical land motion rates, or the overestimations of marshland area measurements. Thus, while the land area projected for the past based on the MSL and the halved subsidence rate can yield valuable insights, it also underscores the need for cautious interpretation and further refinement.

4.3. Land Area Comparison

Following the land area projection for the past years, we studied how the land area decreased during the high water period. Figure 8 illustrates the contrast in land area based on the MSL and MHHW as thresholds.

When considering the MSL, the region adjacent to Bayou des Allemands is predominantly projected as land. However, the same area appears mostly submerged during high waters levels. These contrasting projections offer valuable insights; the MSL-based land area represents an average annual land area, whereas the MHHW-based land area is the portion of the land remaining unaffected by the daily high tide. Nevertheless, it is crucial to note that water highs associated with high tides do not occur simultaneously throughout the region; instead, they are asynchronous as the phase lags relative to ocean tides increase with distance from the coastline. For instance, Zumberge et al. (2022) documented a few hours' phase lag for the diurnal water levels recorded by several CRMS stations separated by a few tens of km in the mid-Barataria region. Thus the time lag of high-waters between different parts of the basin suggests that it is more accurate to consider the MHHW-based land area as the land rarely affected by the high tide throughout the day. Consequently, given that high tides happen at different times across the region, the actual land area at some point during the day should be larger than the MHHW-predicted land area.

4.4. Predicted Land Loss: Implications of Tidal Variations

We predicted how the land area changes of the Barataria region, with a particular emphasis on the impact of MHHW on these areas. From 2017 to 2022, the difference between the predicted MSL land area and the MHHW land area is negligible (Figure 9a and 9b). However, this discrepancy begins to widen considerably by 2045. For the year 2045, the land area prediction based on MHHW with a halved land motion rate accounted for approximately 65% (~1,090 km^2) of the land area predicted using MSL with a halved land motion rate (~1,672 km^2). This estimation was similar to the land area estimated MSL assuming full land motion rate (~1,027 km^2).

This broadening gap between the MSL-based and the MHHW-based land area prediction illustrates the increasing risk of nuisance flooding on land areas, leading to temporary inundation through high tides. For the year 2045 in the lower Barataria region, a significant portion of fragmented marshland persisted, during MSL with a halved vertical land motion rate (Figure 9c). However, during the high tide level, the marsh area is predicted to be almost entirely submerged except for some minor portions of the barrier island. In the upper Barataria region for the same year, the land around Lac des Allemands as well as upper area around Lake Cataouatche and land extends south to the Lake Salvador starts to be submerged during tide highs, in contrast to the land area prediction based on MSL, where most of these lands remain largely the same as in 2022.

This drastic divergence of land area determined by two types of water levels suggests the remaining land area in 2045 may have a height that is very close to MSL, such that small tidal perturbations in the water level could vastly change the land area. Following this scenario, only a small portion of the land area around Lake Salvadro remains emergent during MSL in 2075, while high tides inundate almost the entire region of Barataria (Figure 9d).

5. Conclusions

In this study, we took a comprehensive approach to investigate the coastal inundation and land loss within the Barataria region by considering the impacts of subsidence, sea-level rise, and tidal dynamics. Our analyses illustrate the potential of future land loss without human intervention, with tidal variations becoming a significant factor due to the rise of tidal intrusion. The increasing difference between land area predictions based on MSL and MHHW during the years 2022–2045 highlights the immediate need for effective mitigation strategies to counter the influence of high tides and sea-level rise-related flooding. Our study reinforced the argument that land subsidence, sea level rise, and enhanced tidal intrusion are all important factors driving land loss and elevated flooding risk in the Barataria region. These effects may pose significant threats to other low-lying coastal areas with similar settings. In land loss mapping and flooding risk assessment, the compound effect of these factors should be carefully investigated.

Acknowledgments

This research was supported by start-up funds from University of Houston. The authors express their gratitude to Dr. Torbjörn E. Törnqvist at Tulane University for providing the source for vertical motion data integral to this study. We also acknowledge Brady Couvillion from the United States Geological Survey (USGS) for contributing the geographical data for fastland, which delineated the scope of our analysis and offered valuable insights into the region.

Data Availability Statement

The topobathymetric digital elevation model (TBDEM) utilized in this research is accessible through the USGS EarthExplorer database (https://earthexplorer.usgs.gov/). Vertical land motion data, obtained via Rod Surface Elevation Tables (RSET), are available in Supplementary Data 1 of the publication "Vulnerability of Louisiana's Coastal Wetlands to Present-Day Rates of Relative Sea-Level Rise" (https://www.nature.com/articles/ncomms14792). Quality-assured water elevation measurements, collected from Coastal Restoration Monitoring System (CRMS) tidal gauges, can be accessed via the CRMS network (https://cims.coastal.louisiana.gov/monitoring-data/).

References

Blum, M. D., & Roberts, H. H. (2009). Drowning of the Mississippi Delta due to insufficient sediment supply and global sea-level rise. *Nature Geoscience, 2*(7), 488-491. doi:10.1038/ngeo553

Bowman, P., Perret, W., & Roussel, J. (1995). Freshwater introduction and implications for fisheries production in Louisiana. *Baton Rouge, LA: Department of Wildlife and Fisheries*.

Byrnes, M. R., Britsch, L. D., Berlinghoff, J. L., Johnson, R., & Khalil, S. (2019). Recent subsidence rates for Barataria Basin, Louisiana. *Geo-Marine Letters, 39*(4), 265-278. doi:10.1007/s00367-019-00573-3

Cheng, F. Y., Van Meter, K. J., Byrnes, D. K., & Basu, N. B. (2020). Maximizing US nitrate removal through wetland protection and restoration. *Nature, 588*(7839), 625-630. doi:10.1038/s41586-020-03042-5

Costanza, R., de Groot, R., Sutton, P., van der Ploeg, S., Anderson, S. J., Kubiszewski, I., . . . Turner, R. K. (2014). Changes in the global value of ecosystem services. *Global Environmental Change, 26*, 152-158. doi:https://doi.org/10.1016/j.gloenvcha.2014.04.002

Couvillion, B. R., Beck, H., Schoolmaster, D., & Fischer, M. (2017). *Land area change in coastal Louisiana (1932 to 2016)* (3381). Retrieved from Reston, VA: http://pubs.er.usgs.gov/publication/sim3381

Couvillion, B. R., Fischer, M. R., Beck, H. J., & Sleavin, W. J. (2016). Spatial Configuration Trends in Coastal Louisiana from 1985 to 2010. *Wetlands, 36*(2), 347-359. doi:10.1007/s13157-016-0744-9

CPRA. (2018). *Mid-Barataria and Mid-Breton Sediment Diversions: Overview & Frequently Asked Questions* STATE OF LOUISIANA

CPRA. (2022). *Coastal Information Management System (CIMS) Data Dictionary*. State of Louisiana

Das, A., Justic, D., Inoue, M., Hoda, A., Huang, H., & Park, D. (2012). Impacts of Mississippi River diversions on salinity gradients in a deltaic Louisiana estuary: Ecological and management implications. *Estuarine, Coastal and Shelf Science, 111*, 17-26. doi:https://doi.org/10.1016/j.ecss.2012.06.005

Day, J. W., Britsch, L. D., Hawes, S. R., Shaffer, G. P., Reed, D. J., & Cahoon, D. (2000). Pattern and process of land loss in the Mississippi Delta: A Spatial and temporal analysis of wetland habitat change. *Estuaries, 23*(4), 425-438. doi:10.2307/1353136

Day, J. W., Martin, J. F., Cardoch, L., & Templet, P. H. (1997). System functioning as a basis for sustainable management of deltaic ecosystems. *Coastal Management, 25*(2), 115-153. doi:10.1080/08920759709362315

Edmonds, D. A., Toby, S. C., Siverd, C. G., Twilley, R., Bentley, S. J., Hagen, S., & Xu, K. (2023). Land loss due to human-altered sediment budget in the Mississippi River Delta. *Nature Sustainability*. doi:10.1038/s41893-023-01081-0

Gagliano, S. M., Meyer-Arendt, K. J., & Wicker, K. M. (1981). Land loss in the Mississippi River deltaic plain.

Gornitz, V., White, T. W., & Cushman, R. M. (1991). *Vulnerability of the US to future sea level rise*. Paper presented at the Conference: 7. symposium on coastal and ocean management, Long Beach, CA (USA), 8-12 Jul 1991, United States. https://www.osti.gov/biblio/5875484 https://www.osti.gov/servlets/purl/5875484

Holzer, T. L., & Bluntzer, R. L. (1984). Land Subsidence Near Oil and Gas Fields, Houston, Texasa. *Groundwater, 22*(4), 450-459. doi:https://doi.org/10.1111/j.1745-6584.1984.tb01416.x

Inoue, M., Park, D., Justic, D., & Wiseman, W. J. (2008). A high-resolution integrated hydrology–hydrodynamic model of the Barataria Basin system. *Environmental Modelling & Software, 23*(9), 1122-1132. doi:https://doi.org/10.1016/j.envsoft.2008.02.011

Jankowski, K. L., Tornqvist, T. E., & Fernandes, A. M. (2017). Vulnerability of Louisiana's coastal wetlands to present-day rates of relative sea-level rise. *Nat Commun, 8*, 14792. doi:10.1038/ncomms14792

Karegar, M. A., Dixon, T. H., & Malservisi, R. (2015). A three-dimensional surface velocity field for the Mississippi Delta: Implications for coastal restoration and flood potential. *Geology, 43*(6), 519-522. doi:10.1130/g36598.1

Karegar, M. A., Larson, K. M., Kusche, J., & Dixon, T. H. (2020). Novel Quantification of Shallow Sediment Compaction by GPS Interferometric Reflectometry and Implications for Flood Susceptibility. *Geophysical Research Letters, 47*(14), e2020GL087807. doi:https://doi.org/10.1029/2020GL087807

Mostafiz, R. B., Bushra, N., Rohli, R. V., Friedland, C. J., & Rahim, M. A. (2021). Present vs. Future Property Losses From a 100-Year Coastal Flood: A Case Study of Grand Isle, Louisiana. *Frontiers in Water, 3*. doi:10.3389/frwa.2021.763358

Nelson, S. A. C., Soranno, P. A., & Qi, J. (2002). Land-Cover Change in Upper Barataria Basin Estuary, Louisiana, 1972–1992: Increases in Wetland Area. *Environmental Management, 29*(5), 716-727. doi:10.1007/s00267-001-0060-9

Nienhuis, J. H., Törnqvist, T. E., Jankowski, K. L., Fernandes, A. M., & Keogh, M. E. (2017). A New Subsidence Map for Coastal Louisiana. *GSA TODAY, 27*(9), 2. doi:10.1130/GSATG337GW.1

Pahl, J. (2017). coastal master plan: attachment C-2: eustatic sea level rise. *Coastal Protection and Restoration Authority: Baton Rouge, LA, USA*.

Pawlowicz, R., Beardsley, B., & Lentz, S. (2002). Classical tidal harmonic analysis including error estimates in MATLAB using T_TIDE. *Computers & Geosciences, 28*(8), 929-937. doi:https://doi.org/10.1016/S0098-3004(02)00013-4

Poulter, B., & Halpin, P. N. (2008). Raster modelling of coastal flooding from sea-level rise. *International Journal of Geographical Information Science, 22*(2), 167-182. doi:10.1080/13658810701371858

Roberts, H. H. (1997). Dynamic Changes of the Holocene Mississippi River Delta Plain: The Delta Cycle. *Journal of Coastal Research, 13*(3), 605-627. Retrieved from http://www.jstor.org/stable/4298659

Sweet, W., Dusek, G., Obeysekera, J. T. B., & Marra, J. J. (2018). Patterns and projections of high tide flooding along the U.S. coastline using a common impact threshold. doi:http://doi.org/10.7289/V5/TR-NOS-COOPS-086

Thompson, P. R., Widlansky, M. J., Hamlington, B. D., Merrifield, M. A., Marra, J. J., Mitchum, G. T., & Sweet, W. (2021). Rapid increases and extreme months in projections of United States high-tide flooding. *Nature Climate Change, 11*(7), 584-590. doi:10.1038/s41558-021-01077-8

Törnqvist, T. E. (2023). A river delta in transition. *Nature Sustainability, 6*(6), 617-618. doi:10.1038/s41893-023-01104-w

USACE. (2022). *Environmental Impact Statement For The Propose Mid-Barataria Sediment Diversion Project*.

USGS. (2018). *USGS EROS Archive - Digital Elevation - Coastal National Elevation Database (CoNED) Project - Topobathymetric Digital Elevation Model (TBDEM)* [gif].

Vaccare, J., Meselhe, E., & White, J. R. (2019). The denitrification potential of eroding wetlands in Barataria Bay, LA, USA: Implications for river reconnection. *Science of The Total Environment, 686*, 529-537. doi:https://doi.org/10.1016/j.scitotenv.2019.05.475

Yang, Z., Wang, T., Leung, R., Hibbard, K., Janetos, T., Kraucunas, I., . . . Wilbanks, T. (2014). A modeling study of coastal inundation induced by storm surge, sea-level rise, and subsidence in the Gulf of Mexico. *Natural Hazards, 71*(3), 1771-1794. doi:10.1007/s11069-013-0974-6

Yunus, A., Avtar, R., Kraines, S., Yamamuro, M., Lindberg, F., & Grimmond, C. (2016). Uncertainties in Tidally Adjusted Estimates of Sea Level Rise Flooding (Bathtub Model) for the Greater London. *Remote Sensing, 8*(5). doi:10.3390/rs8050366

Zumberge, M. A., Xie, S., Wyatt, F. K., Steckler, M. S., Li, G., Hatfield, W., . . . Törnqvist, T. E. (2022). Novel Integration of Geodetic and Geologic Methods for High-Resolution Monitoring of Subsidence in the Mississippi Delta. *Journal of Geophysical Research: Earth Surface, 127*(9), e2022JF006718. doi:https://doi.org/10.1029/2022JF006718

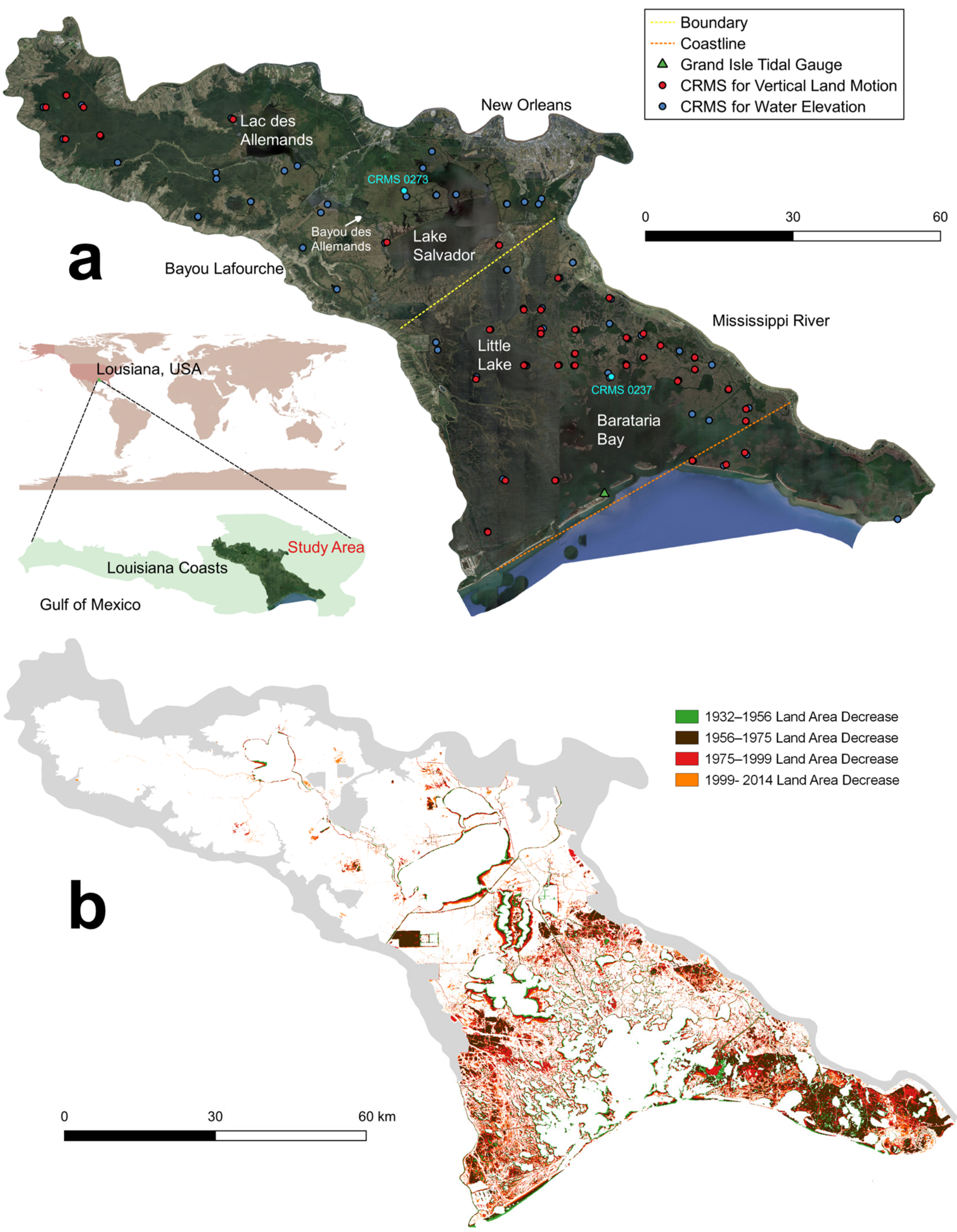

Figure 1. Map of the study area. (a) The Barataria Basin along the Louisiana coast, showcasing the exclusion of fast land areas (developed or protected zones) from the study. The regional mask for the study area was sourced from the USGS. (b) Persistent land loss from 1932 to 2014 (Couvillion et al., 2017).

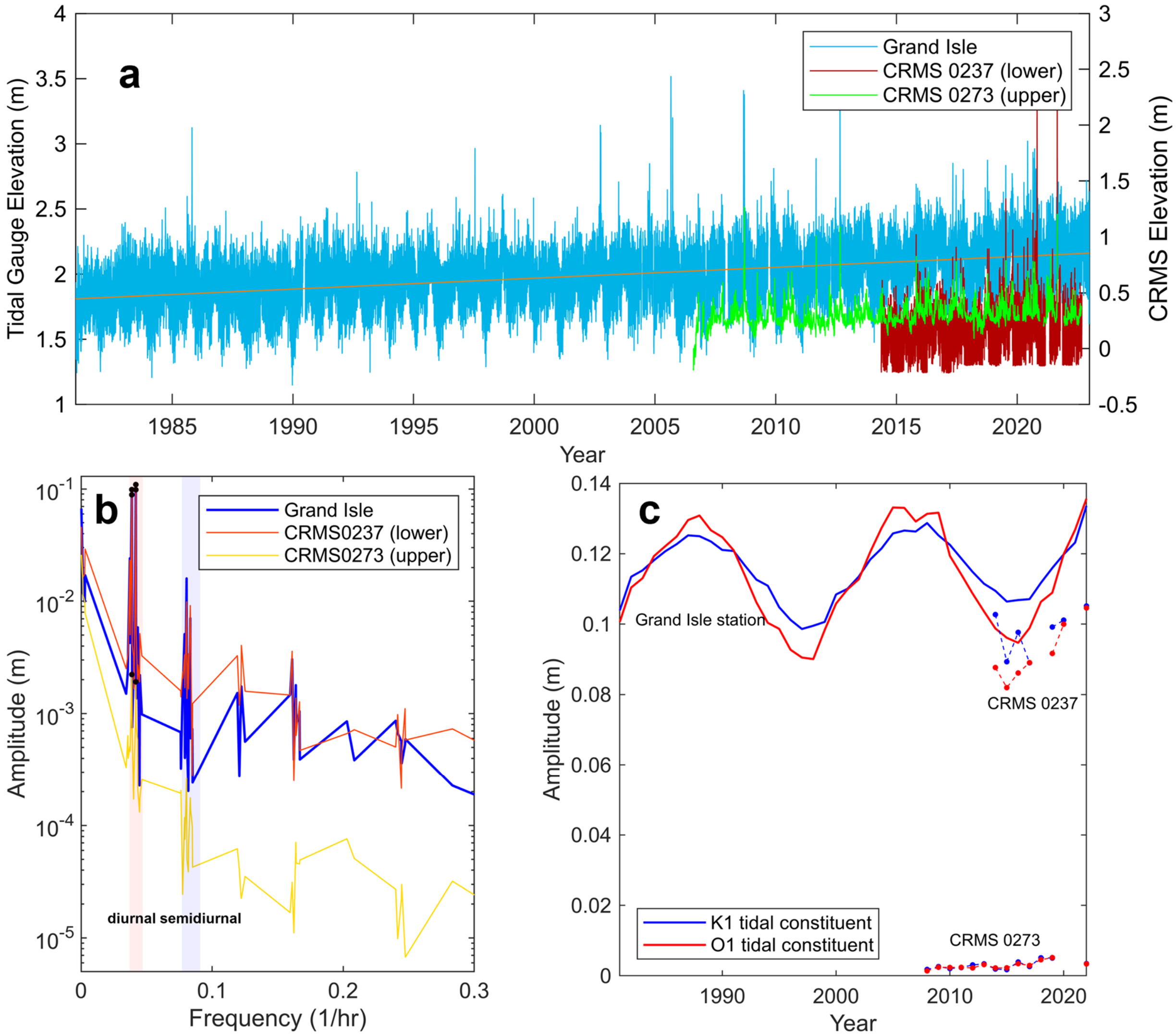

Figure 2. Tidal characteristics of the Barataria Basin. (a) Time series depicting fluctuations in water elevation at the Grand Isle tidal gauge and CRMS Stations: The Grand Isle measurements, referenced to the station datum, are influenced by both sea level rise (SLR) and land subsidence. Conversely, CRMS data, referenced to NAVD 88, are solely affected by SLR, as instrumental drift has been adjusted. (b) Tidal spectrum from the Grand Isle tidal gauge and CRMS stations in 2014, highlighting the peak constituents O1 and K1. (c) Amplitude of the diurnal tide constituents of water elevation, as observed at the Grand Isle tidal gauge from 1981 to 2022.

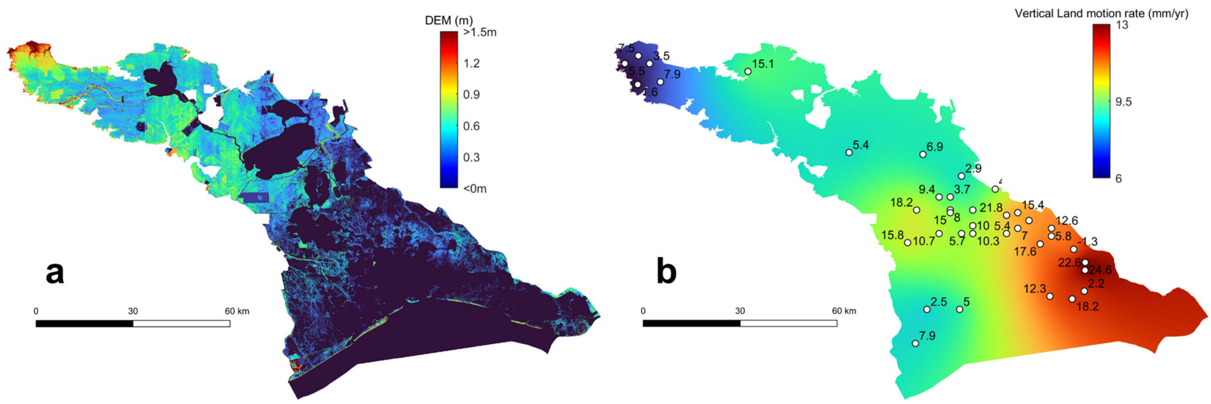

Figure 3. DEM and vertical land motion rates in the Barataria Basin. (a) Topobathymetric digital elevation models for the Barataria region (USGS, 2018). (b) Map illustrating vertical land motion rates based on Kriging interpolation of data from Jankowski et al. (2017). The geostatistical interpolation method applied aligns with the approach described in Nienhuis et al. (2017).

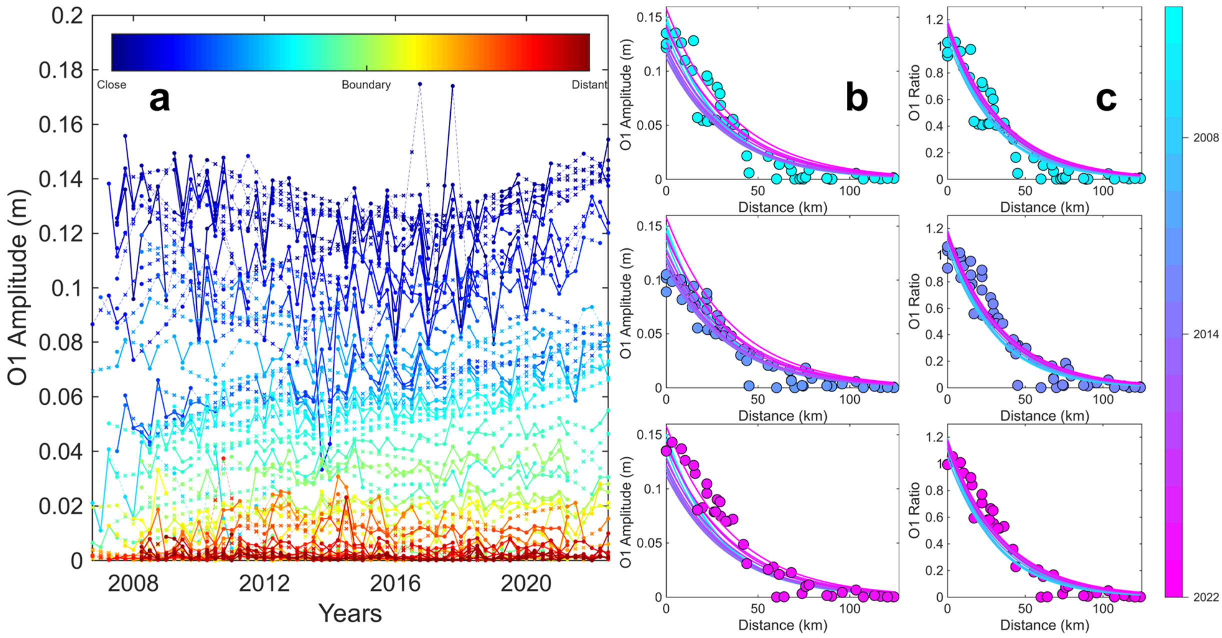

Figure 4. Tidal amplitude variations. (a) The graph depicts amplitude of O1 tidal constituents, for each quarter from 2006 to 2022 across various CRMS stations, with color grading indicating the relative order of their distances from coastlines. The 'x' symbols represent interpolated values, filling gaps in actual data points represented by dot symbols. For stations located on the seaward side of the coastline, the distance from the coastline is considered as zero. The nearest distance from each CRMS station to a coastline segment (see Figure 1a) was calculated assuming a spherical Earth model. (b - c) The scattered dots represent the annual O1 amplitudes and ratios in terms of the distance from the coastline for the years 2008, 2014, and 2022. The amplitude ratios are determined by the annual O1 amplitudes for CRMS divided by the annual O1 amplitude for the Grand Isle tidal gauge. The exponential trend lines, differentiated by color,

illustrate the exponential regression fits for these data points, with each color corresponding to a specific year.

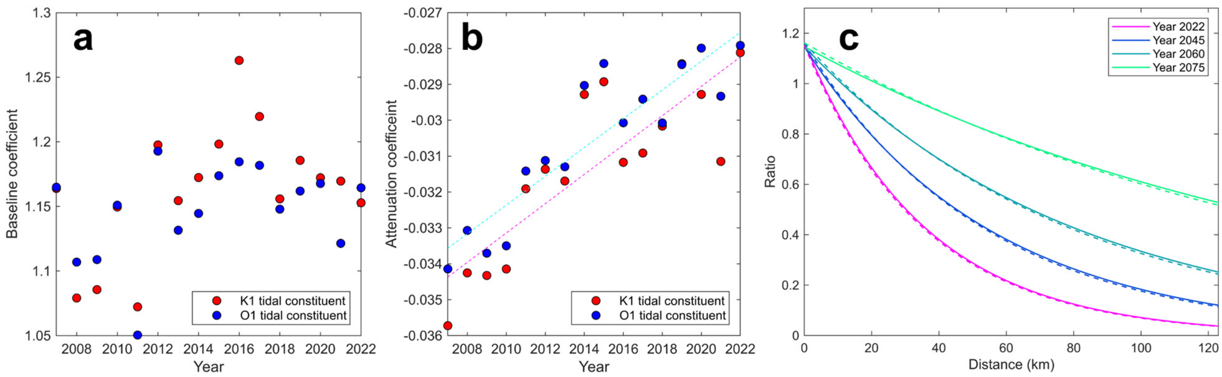

Figure 5. Annual baseline coefficients α (a) and annual attenuation coefficients β (b) for exponential regression fit for O1 and K1 amplitude ratios. A linear regression of these annual baseline coefficients showed no significant trend (p-value was 0.07 for K1, and 0.21 for O1 constituents; with R-squared values 0.22 and 0.11). In contrast, the annual attenuation coefficients for both constituents exhibited a significant linear trend (p-value of 0.0004 for K1, and 0.00002 for O1; R-squared values of 0.71 and 0.81). (c) Predicted future ratios for O1(solid line) and K1(dotted line) are also shown with regards to distances.

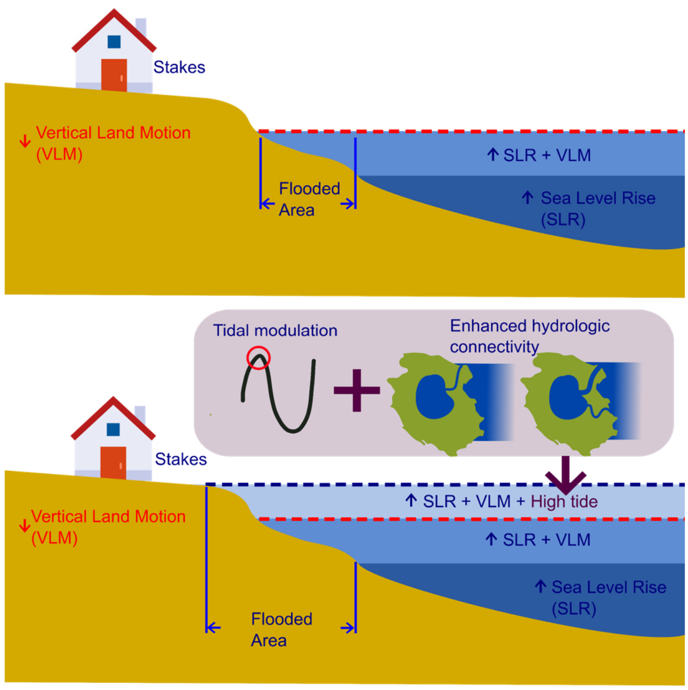

Figure 6. Conceptual diagram illustrating the widening of areas affected by nuisance flooding during high tides.

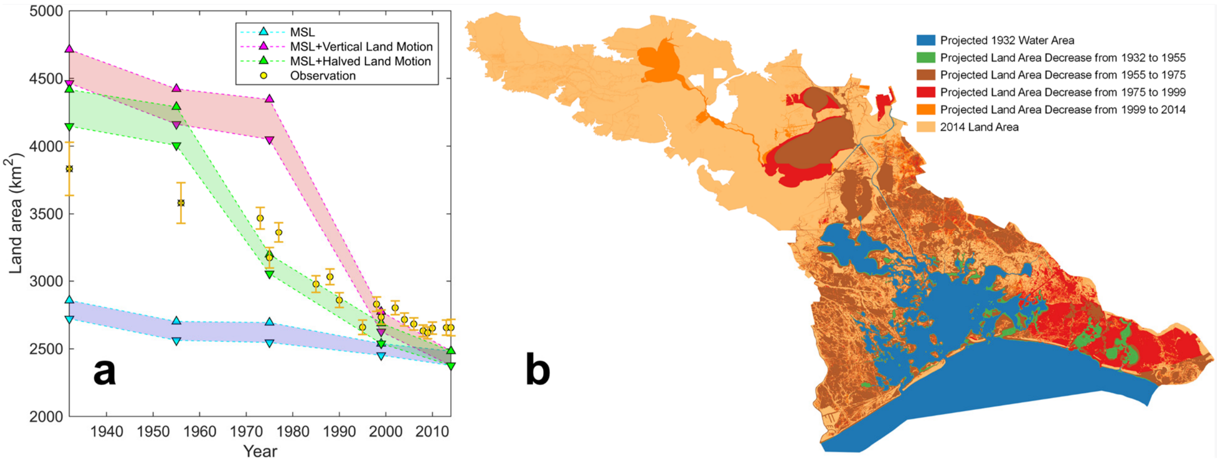

Figure 7. Projection of land area change. (a) Changes in land area from 1932 to 2014. The triangles represent land area projections based on four-pixel connectivity, whereas the inverted-triangles illustrate projections that zero-pixel connectivity. Land area measurements derived from surveys and aerial photos from 1932 and 1955 are marked with the 'x' symbols, while Landsat measurements are included as references (Couvillion et al., 2017). Confidence bounds were calculated using 1.96 for the standard error. (b) Projections of land changes from 1932 to 2014 based on MSL and the halved land motion rate.

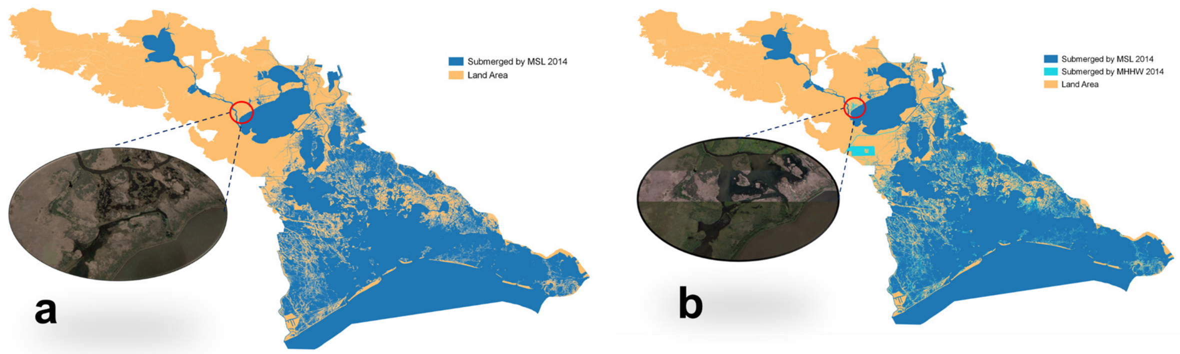

Figure 8. Distribution of land and sea areas on MSL and MHHW in 2014. Satellite images from January 2015 (a) and October 2014 (b) illustrate how land can transition between emergent and submerged states due to variations in water level.

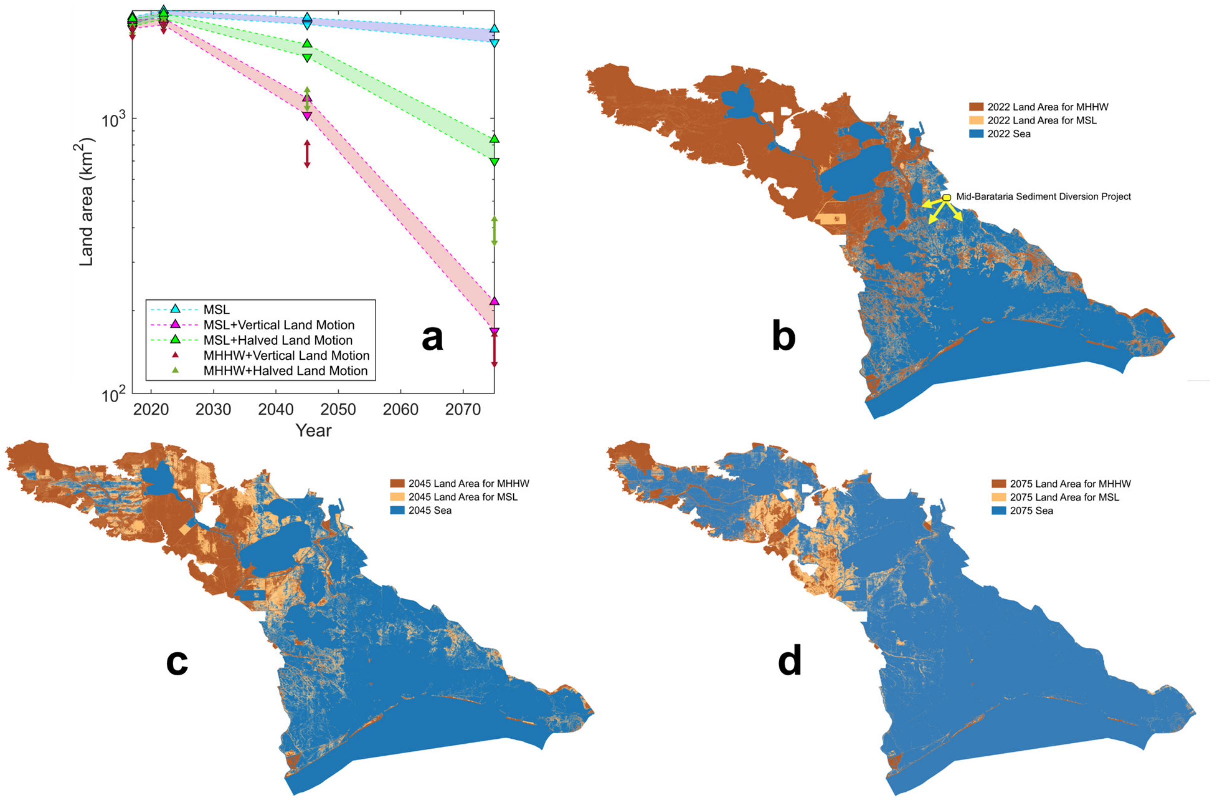

Figure 9. Prediction of land area from 2017 to 2075. In (a), the triangles symbolize the land area projection based on 4-way hydro-connectivity, while the inverted-triangles represent projections without considering connectivity. (b-d) Distribution of land and sea areas for the years 2022, 2045, and 2075 respectively. All land estimations were calculated assuming a rate of vertical motion reduced by half. The location of Mid-Barataria Sediment Diversion (MBSD) project is also shown as a reference in panel (b).